Applied Catalysis B: Environmental 193 (2016) 36–46

Contents lists available at ScienceDirect

Applied Catalysis B: Environmental

journal homepage: www.elsevier.com/locate/apcatb

Facile synthesis of Sb_2S_3/ultrathin g-C_3N_4 sheets heterostructures embedded with g-C_3N_4 quantum dots with enhanced NIR-light photocatalytic performance

Hui Wang[a,b], Xingzhong Yuan[a,b,*], Hou Wang[a,b], Xiaohong Chen[c], Zhibin Wu[a,b], Longbo Jiang[a,b], Weiping Xiong[a,b], Guangming Zeng[a,b]

[a] College of Environmental Science and Engineering, Hunan University, Changsha 410082, PR China
[b] Key Laboratory of Environment Biology and Pollution Control, Hunan University, Ministry of Education, Changsha 410082, PR China
[c] Hunan University of Commerce, Changsha 410205, PR China

ARTICLE INFO

Article history:
Received 23 January 2016
Received in revised form 25 March 2016
Accepted 31 March 2016
Available online 1 April 2016

Keywords:
CNQD
utg-C_3N_4
Sb_2S_3
Near-infrared
Photocatalysis

ABSTRACT

In recent years, exploiting novel photocatalysts with a broad range of wavelengths photoresponse is undoubtedly interesting in photocatalytic field. Here, a novel Sb_2S_3/ultrathin g-C_3N_4 sheets heterostructures embedded with g-C_3N_4 quantum dots (CNS) was successfully fabricated via a facile hydrothermal process. The samples were systematically characterized by the field emission scanning electron microscopy (FESEM), transmission electron microscopy (TEM), X-ray diffraction (XRD), X-ray photoelectron spectroscopy (XPS), UV–vis-NIR diffuse reflection spectroscopy (UV-vis-NIR DRS) and photoluminescence (PL) spectroscopy. It is indicated that the composites have fast electron transport and enhanced solar light absorption. Moreover, the CNS composite exhibits a significant photoelectric conversion property in near-infrared (NIR) wavelength range. The photocatalytic activities of the samples were evaluated by the degradation of methyl orange (MO) upon NIR irradiation. The photodegradation rate of the optimal CNS for MO was 0.0103 min^{-1}, about 2.6 times higher than that of pure Sb_2S_3. The improved NIR photocatalytic activity may base on the improved absorption in the NIR region, efficient electron-hole separation and the up-converted PL property of g-C_3N_4 quantum dots (CNQD).

1. Introduction

Solar energy, as a clean and inexhaustible resource, has long been regarded as one of the most promising renewable clean energy sources for environmental pollutants degradation [1–3]. In view of efficient solar energy conversion, exploiting a semiconductor photocatalysts that can harvest wide spectrum of solar light, from ultraviolet (UV) to near-infrared (NIR) wavelength, undoubtedly remains an urgent challenge for high solar energy conversion [4,5]. However, only a few NIR photocatalysts have been investigated, such as up-conversion materials involving the rare earth element, carbon materials quantum dots and carbon nitride quantum dots [6–9]. The up-conversion property can make the photocatalysts absorb NIR light and emit visible light. Hence, it is desirable to exploit promising photocatalysts that could efficiently harvest the visible or even NIR light.

Antimony trisulfide (Sb_2S_3), a significant V-VI semiconductor, possesses unique properties such as chain-like layered structure, good photosensitivity and high thermoelectric power [10,11]. Notably, it has a suitable band gap, which matches closely the maximum scan from the visible to near-infrared region of the solar spectrum [12,13]. These properties make Sb_2S_3 receive significant attention for potential applications involving solar cells [14], photosensors [15], lithium ion batteries [16], thermoelectric and optoelectronic devices [17]. However, it still could not meet the requirements for practical application due to the low photoelectric conversion efficiency. Numerous strategies have been employed to improve the photocatalytic properties of pure Sb_2S_3. Particularly, integrating Sb_2S_3 with other semiconductors to form heterojunctions was proved to be an effective and feasible strategy. Recently, Sb_2S_3-based composites, such as graphene-Sb_2S_3 [17], Ag_2S/Sb_2S_3, [18], CdS/Sb_2S_3 [19], and TiO_2/Sb_2S_3 [20] etc., have been developed to enhance the photocatalytic activity. However, it still suffers

* Corresponding author at: College of Environmental Science and Engineering, Hunan University, Changsha 410082, PR China.
E-mail address: yxz@hnu.edu.cn (X. Yuan).

http://dx.doi.org/10.1016/j.apcatb.2016.03.075
0926-3373/

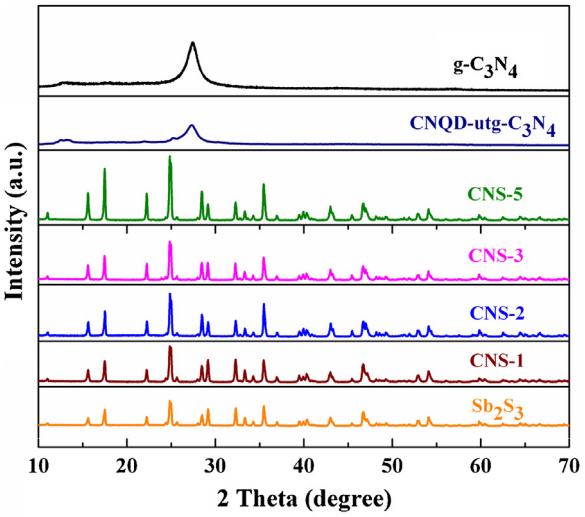

Fig. 1. XRD patterns for g-C_3N_4, CNQD-utg-C_3N_4 and CNS composites.

from some limitations including high cost, complicated synthesis process, or instability during photochemical operations.

Different from metal compound photocatalyst, graphite-like carbon nitride (g-C_3N_4), a nontoxic metal-free semiconductor can be synthesized by a simple heating of urea [21], cyanamide [22], or melamine [23]. In addition, g-C_3N_4 possesses a stacked 2D structure and outstanding optical, thermal and electrical characteristics [24]. These unique properties make the metal-free g-C_3N_4 have great potentiality in the field such as bioimaging [25], gas storage [26], photovoltaic and photocatalytic fields [27]. Nevertheless, bulk g-C_3N_4 is still limited by the relatively small specific surface area, low photoresponsivity and poor solubility [28–30]. Recently, 2-D ultrathin nanosheets (utg-C_3N_4) have been successfully obtained by exfoliating the counterparts into a single atomic layer [31]. Compared with bulk g-C_3N_4, the utg-C_3N_4 nanosheets with atomic-scale thickness possess a graphite-like lamellar structure and high specific surface area, which can facilitate the photoresponse and the charge transfer [32]. However, an examination in the available examples revealed that almost all of them are still only applied in the visible light range. To further improve the photocatalytic efficiency, it is imperative to fabricate the utg-C_3N_4-based photocatalysts that can be active in NIR light.

Our group has reported novel g-C_3N_4/$NiTiO_3$ [33], g-C_3N_4/MIL-125(Ti) [34], g-C_3N_4-Sb_2S_3/$Sb_4O_5Cl_2$ [35] and SnS_2-$MgFe_2O_4$/GO heterostructures [36], which demonstrated enhanced visible light photocatalytic activities. In this article, a simple and environmental hydrothermal method, based on the reactions of antimony trichloride and sodium sulfide, was employed to prepare novel CNS heterojunctions. The obtained photocatalysts were characterized by means of FESEM, TEM, XRD, XPS, UV–vis-NIR DRS and PL spectroscopy. By optimizing the compositions, an optimum composite was found and showed improved photocatalytic activities towards methylene orange (MO) under UV, visible and NIR irradiation in comparison with pure Sb_2S_3. The possible photocatalytic mechanism as well as the reusability and stability of the photocatalyst were also investigated.

2. Experimental

2.1. Materials

Sodium sulfide ($Na_2S{\cdot}9H_2O$, 98%), antimony chloride ($SbCl_3$, 100%), sodium hydroxide (NaOH, 98%), hydrochloric acid (HCl, 36%-38%) were purchased from Sinopharm Chemical Reagent Co., Ltd (Shanghai, China). Methylene orange was supported by Tianjin Damao Chemical Reagent Co, Ltd (Tianjin, China). All other reagents and solvents were of analytical reagent grade and used as received from commercial suppliers.

2.2. Preparation of CNS hybrid materials

The g-C_3N_4 was prepared by calcination with dicyandiamide as precursor. 10 gdicyandiamide was put into a covered crucible, and heated at 550 °C in a muffle furnace for 2 h. The yellow g-C_3N_4 powders were obtained after cooling. In brief, 1 g g-C_3N_4 powder was dispersed in 150 ml water and then subjected to ultrasound continuously for 10 h. Finally, the suspension was centrifuged at 3000 rpm for 10 min to remove byproducts of large particles, and then the supernatant containing ultrathin g-C_3N_4 sheets embedded with g-C_3N_4 quantum dots (CNQD-utg-C_3N_4) was collected.

A certain amount CNQD-utg-C_3N_4 was dispersed into 50 ml NaOH solution, and 5 mmol $Na_2S{\cdot}9H_2O$ was added to obtain solution A. In another beaker solution 2 was prepared by dissolving equal molar ratio of antimony chloride ($SbCl_3$) in 25 ml HCl solution. Finally, solution 2 was added drop by drop to solution 1 with the aid of stirring, and transferred to a Teflon-lined stainless-steel autoclave for 12 h at 100 °C. The obtained precipitate was collected after washing with distilled water and dried at 60 °C in an oven for 12 h. The as-prepared CNS samples with expected CNQD-utg-C_3N_4 volume of 10, 35 and 50 ml were labeled as CNS-1, CNS-3, CNS-5, respectively. As reference, normal Sb_2S_3 was synthesized via the same strategy but without the addition of CNQD-utg-C_3N_4.

2.3. Characterization

The powder X-ray diffraction (XRD) patterns were recorded using Bruker AXS D8 Advance diffractometer equipped with Cu-K*a* source ($\lambda = 1.541$ Å). The morphologies of samples were characterized by a field emission scanning electron microscopy (SEM) (JSM-7001F, Japan) and transmission electron microscopy (TEM) (JES-3010, Japan). The X-ray Photoelectron Spectroscopy spectrum (XPS) (Thermo Fisher Scientific, UK) was carried out to analyze the surface elemental composition analyses. UV-vis-NIR diffuse reflectance spectra (DRS) of the samples were recorded on a UV-vis-NIR spectrophotometer (U-4100, Hitachi, Japan) with an integrating sphere attachment within the range of 240–2600 nm. Steady-state photoluminescence (PL) spectra were examined by Perkin-Elmer LS-55 spectrofluorimeter. The up-convertion PL specttra was detected by a Jobin Fluorolog-3-P fluorescent spectrometer coupled with a NIR laser at $\lambda = 980$ nm as the excitation source. Photocurrent measurements were performed on a CHI 660D electrochemical workstation (Shanghai Chenhua, China) using a three-electrode cell with the nanostructure materials on FTO as the working electrode, saturated Ag/AgCl and platinum electrode as the counter electrode and the reference electrode, respectively.

2.4. Photocatalytic activity measurement

Photocatalytic degradation of MO was conducted vertically irradiated by a 300 W xenon lamp (Beijing China Education Au-light Co. Ltd) with a cutoff filter ($\lambda \geq 420$ nm) or ($\lambda \geq 760$ nm). The light source (14 V, 16 A, 15 cm) far away from the photocatalytic reactor. Typically, 100 mg powdered catalysts were dispersed in 100 ml of 10 mg/L MO solution. Then, the solution was magnetically stirred for 1 h in darkness to attain adsorption equilibrium. Aliquots were drawn out of the solution at defined time intervals, centrifuged, and examined at 463 nm using a UV–vis spectrophotometer (UV-2250, SHIMADZU Corporation, Japan). The MO concentration after adsorption equilibrium is acted as the initial concentration (C_0). Five successive cyclic tests were implemented over the optimal

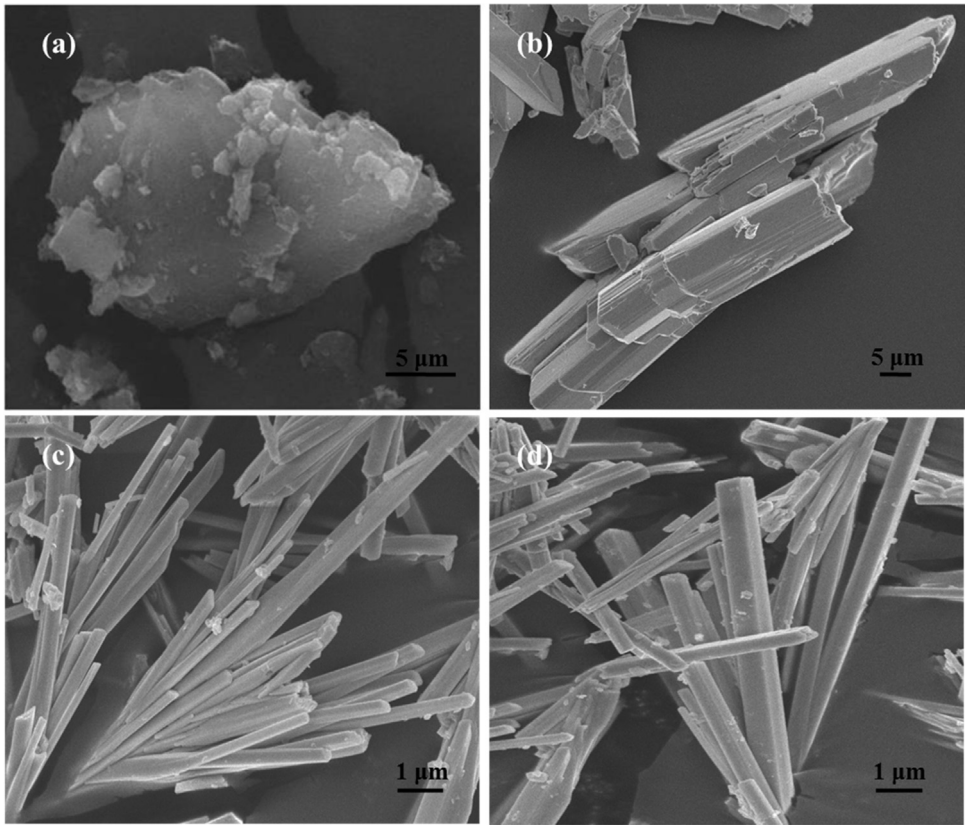

Fig. 2. SEM image of g-C_3N_4 (a), Sb_2S_3 (b) and CNS-3 (c–d).

hybrid as follows. After the every run, the sample was washed several times with deionized water, dried at 60 °C in air and subjected to the next run.

3. Results and discussion

3.1. Characterization

The purity and crystallinity of the parent materials and hybrids were confirmed by XRD shown in Fig. 1. The peak of g-C_3N_4 at 27.2° is attributed to the stacking peak of π-conjugated layers, corresponding to the typical facets (002) [37]. After exfoliation, the CNQD-utg-C_3N_4 only reveals a weak (002) peak, demonstrating that layered g-C_3N_4 has been successfully exfoliated as expected. It can be seen that the characteristic peaks of the as-prepared Sb_2S_3 match well with those reported (JCPDS file 42–1393) in the literatures [17,38,39], which include (020), (120), (220), (130), (230), (211), (221), (240), (421), (501), (332) and (132) plans. Additionally, no other characteristic peaks of any impurity phase are observed, such as antimony oxides, confirming the high crystallinity of Sb_2S_3. As for the CNS composites, most diffraction peaks are consistent with that of Sb_2S_3, and no defined impurity peaks are detected, indicating that the Sb_2S_3 structure remains unchanged in the hydrothermal process. Additional, no obvious diffraction peak of CNQD-utg-C_3N_4 could be discerned here, probably due to the small amounts of CNQD-utg-C_3N_4 introducing and high dispersion in the composites.

The morphology and structural changes of the samples characterized via SEM, TEM, and HRTEM. As displayed in Fig. 2a, bulk g-C_3N_4 sample presents aggregated morphologies consisting of irregular block-based flakiness and particles [40]. Fig. 2b shows a typical SEM image of the Sb_2S_3 rods with smooth surfaces, which are 3–10 μm in width, 10–50 μm in thickness. After introducing CNQD-utg-C_3N_4, surface-coarsened CNS nanorods are obtained (Fig. 2c–d). It is worth noting that the morphology and size of the CNS hybrid is significantly different to pure Sb_2S_3, the components of which are of diverse shapes and a larger size. It can be seen that the agglomeration morphology and the attachment of CNQD-utg-C_3N_4 with different shapes on the rough surfaces of Sb_2S_3 rods. This clearly exhibits that adding the CNQD-utg-C_3N_4 could lead to the appearing of very small sheaf-like Sb_2S_3 rods which decreased to 100–500 nm and tied together. It is indicated that the presence of CNQD-utg-C_3N_4 controls the crystallization and morphology of Sb_2S_3. Moreover, the CNQD-utg-C_3N_4 nanoparticles became smaller when compared with the bulk g-C_3N_4, which confirmed the successfully exfoliating of g-C_3N_4.

In the TEM images (Fig. 3), the apparent microscopy contrast further confirms the presence of CNQD-utg-C_3N_4 nanosheets on the surface of Sb_2S_3 microrods. The bulk g-C_3N_4 (Fig. 3a) displays two dimensional and overlaps lamellar structures. The CNS heterostructures (Fig. 3b–c) retain a one-dimensional morphology, and the Sb_2S_3 nanorods are surrounded by a thin layer of CNQD-utg-C_3N_4 shells. As shown in Fig. 3d, the small CNQD appear in the utg-C_3N_4 nanosheets, and the observed diameters of CNQD are less than 10 nm. There are relevant reports on quantum dots obtained by ultrasonic method, such as carbon quantum dots, grapheme quantum dots, carbon nitride quantum dots and MoS_2 quantum dots [8,41–43]. Additionally, the cross-sectional atomic force microscopy (AFM) is further conducted to investigate the structural features of the CNQD-utg-C_3N_4 heterostructures (Fig. 4a). Randomly measured nanosheets shows a thicknesses of only 1.3 nm (Fig. 4b), indicating the exfoliated nanosheets consisted of less than five C-N layers [29]. High-resolution TEM (HRTEM) analysis revealed the highly crystalline features of the Sb_2S_3 nanorods, with a lattice spacing of 0.58 nm (Fig. 3e), which can be assigned to the (131) plane of the orthorhombic Sb_2S_3. It can be seen that

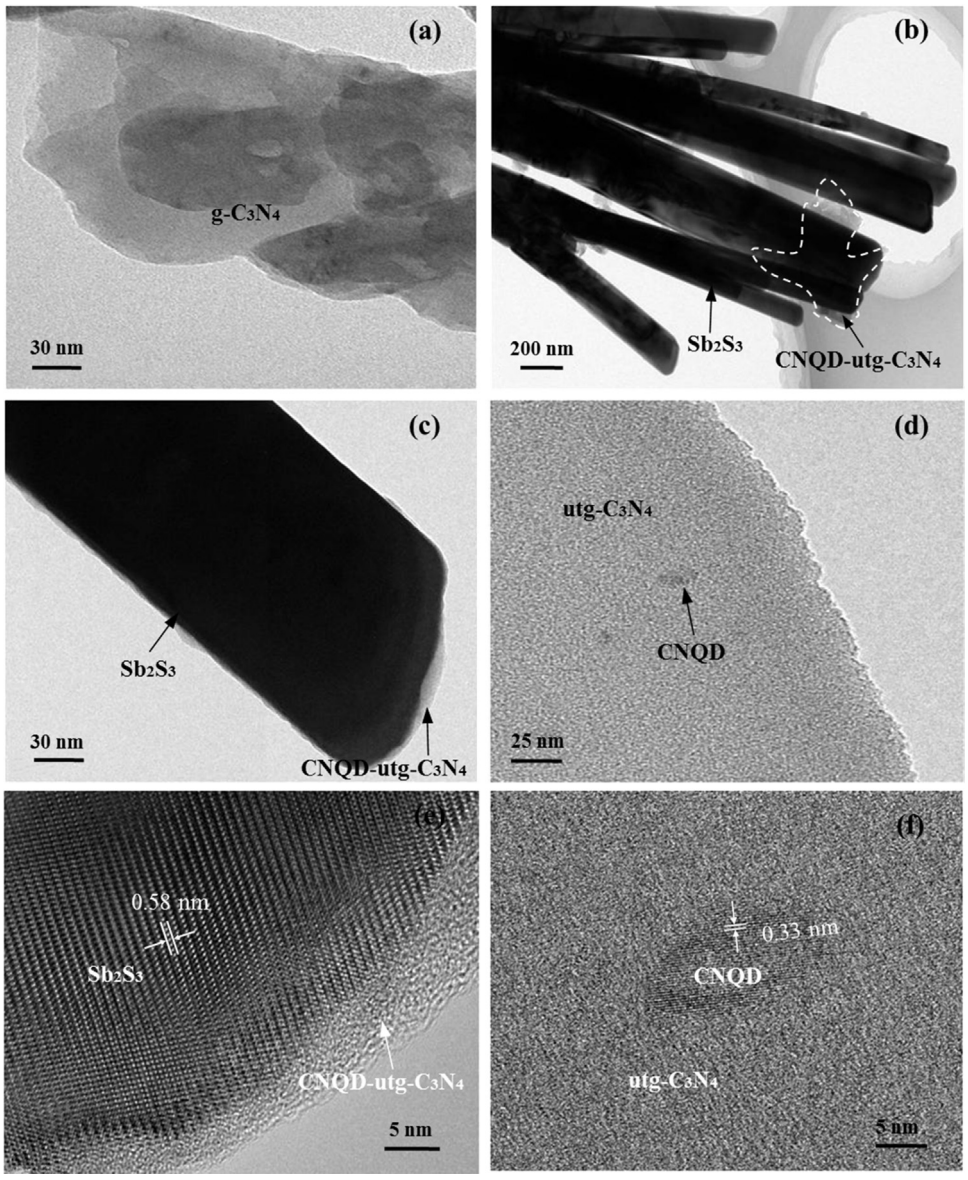

Fig. 3. TEM images of g-C_3N_4 (a), CNS-3 (b and c) and corresponding HRTEM images.

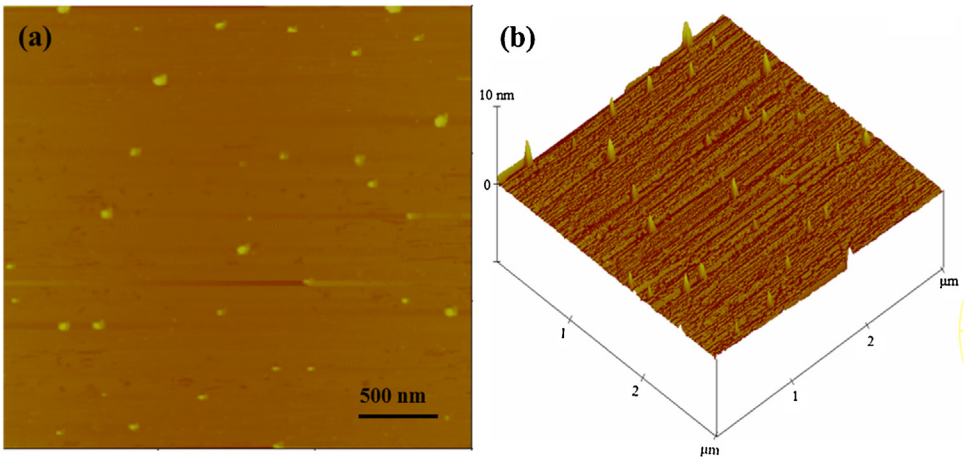

Fig. 4. AFM image of CNQD-utg-C_3N_4 (a) and corresponding 3D height profile (b).

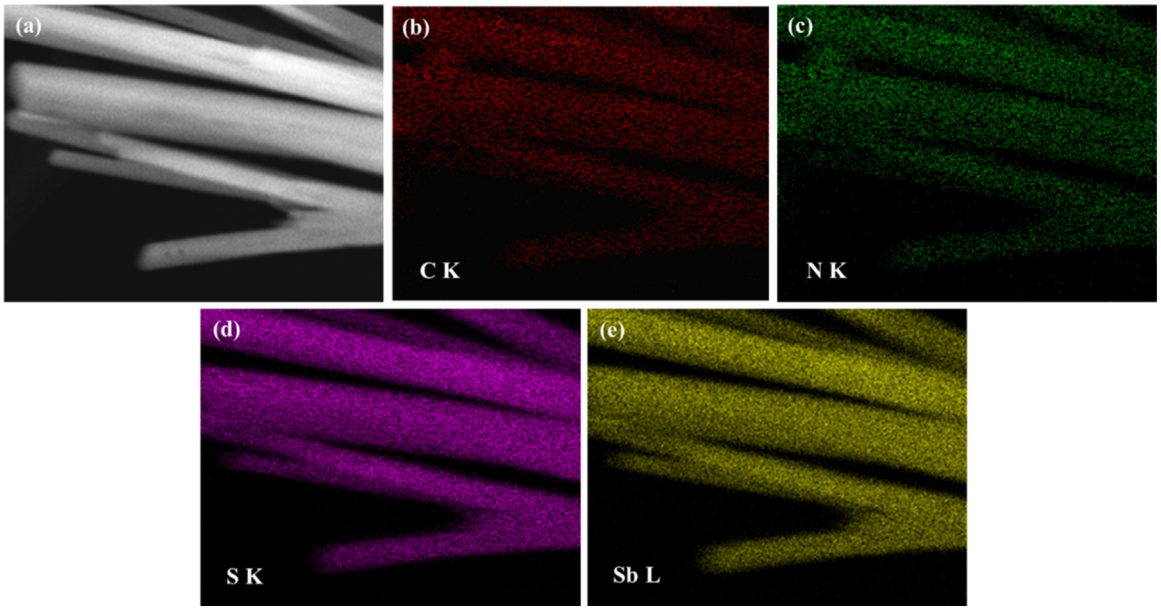

Fig. 5. TEM image of CNS-3 (a) and corresponding elemental mapping images (b–e).

the amorphous phase around Sb_2S_3 nanorods corresponds to the utg-C_3N_4. On the other hand, the measured interplanar spacing of CNQD is 0.333 nm (Fig. 3f), coinciding with the (002) spacing of carbon nitride [44]. TEM element mapping (Fig. 5a–e) also shows the corresponding distribution of various elements. It is clearly found that C, N, Sb and S elements are uniformly dispersed in specific portion selected, further verifying the formation of CNS hybrids. Based on the above analyses, it can be confirmed that the heterojunction between Sb_2S and ultrathin g-C_3N_4 sheets heterostructures embedded with g-C_3N_4 quantum dots forms, which expects to facilitate the transfer of photo-generated charge carriers.The X-ray photoelectron (XPS) spectra were taken to probe the surface elemental composition and electronic structure of Sb_2S_3 and CNS-3. Fig. 6a represents a survey spectrum, indicating the peaks of C, N, S and Sb element in CNS-3 and no obvious impurities could be detected. The CNS-3 sample exhibits S 2p and Sb 3d signals with a S/Sb ratio of 1.56, which is very close to stoichiometric ratio of Sb_2S_3. High-resolution spectra of C1s (Fig. 6b) at 284.4 eV and 288.3 eV are assigned to the C—C bonds and the tertiary carbon C-$(N)_3$ [45–47]. The N 1s spectrum of CNS-3 sample (Fig. 6c) displays three peaks centering at 399.8, 400.1, and 405.1 eV. The N 1s contributions at 399.8 and 400.1 eV can be assigned to N atoms sp^2-bonded to two carbon atoms (C═N—C) and bridging nitrogen atoms N-$(C)_3$, respectively [48,49]. In the Sb 3d spectra (Fig. 6d), peaks at 529.8 eV and 539.1 eV for Sb_2S_3 are attributed to Sb $3d_{5/2}$ and Sb $3d_{3/2}$, respectively, indicating that antimony bounded to sulphur remains in Sb^{3+} oxidation state [17,50]. Those peaks in the spectrum of CNS-3 shift to 530.3 eV and 539.6 eV, respectively, being 0.5 eV higher than those of Sb_2S_3. Fig. 6e shows S 2p spectra of Sb_2S_3 in comparison with that of CNS-3. The binding energy values of pure Sb_2S_3 at 161.6 eV and 162.7 eV, corresponded to the S $2p_{3/2}$ and S $2p_{1/2}$, which can be ascribed to a single doublet from S-Sb bonds [51]. While the shift of 0.5 eV to the higher binding energies of 162.1 and 163.2 V, respectively, is observed for CNS-3. The spin-orbit separations of S are found to be 1.1 eV, indicating that the S is present as S^{2-} in the sample [52]. The shift order of S 2p energy position is the same as that of the Sb 3d peak position, which could be explained by the interaction between CNQD-utg-C_3N_4 and Sb_2S_3, or the formation of CNS heterojunctions. In addition, the binding energy shifts occurring on the XPS spectra may be attributed to the electron transfer between the Sb_2S_3 and CNQD-utg-C_3N_4 nanosheets due to their different electron concentration. Considering the XRD patterns, SEM, TEM and XPS, it can be inferred that the CNS composite has been successfully synthesized.

Table 1
Values of band gap energy (Eg) and corresponding CB (E_{CB}) and VB (E_{VB}) edge positions of as-prepared samples.

Samples	E_g(eV)	$E_{VB}(V_{NHE})$	$E_{CB}(V_{NHE})$
Sb_2S_3	1.26	1.76	0.5
CNS-1	1.45	1.86	0.41
CNS-3	1.36	1.81	0.45
CNS-5	1.50	1.88	0.38
g-C_3N_4	2.70	1.57	−1.13
CNQD-utg-C_3N_4	2.60	1.52	−1.08

3.2. Optical and photoelectrochemical properties

The UV–vis-NIR DRS analysis was implemented to determinate the optical property of as-prepared g-C_3N_4, CNQD-utg-C_3N_4, Sb_2S_3 and CNS composites. From Fig. 7, the absorption spectrum of CNQD-utg-C_3N_4 nanosheets extends to the whole visible light region and even the infrared region compared with the bulk g-C_3N_4. It clearly reveals that the Sb_2S_3 exhibits an optical absorption in the region of 300–1000 nm. After the assembling of CNQD-utg-C_3N_4 nanosheets, the CNS hybrids not only extend to the NIR absorption but also exhibit enhanced absorption intensity in the whole solar region. The phenomenon clearly indicates that coupling CNQD-utg-C_3N_4 is beneficial to improve the light absorption of Sb_2S_3, particularly in the NIR light, implying the enhanced photocatalytic activity.

The band gap energy (*Eg*) of g-C_3N_4, CNQD-utg-C_3N_4, Sb_2S_3 and the CNS-3 composite can be estimated, respectively, according to Eq. (1) and the diagram is shown in Fig. 8.

$$E_g = 1240/\lambda \quad (1)$$

where λ is the wavelength (nm) of the absorption edge [53]. The band gap energies (E_g) of as-prepared photocatalysts are presented in Table 1. Compared with pure Sb_2S_3, the band gap energy of CNS-3 increases due to the introduction of CNQD-utg-C_3N_4, and thus improving the light responses. Moreover, the valence band (VB) edge position and the conduction band (CB) edge position of the

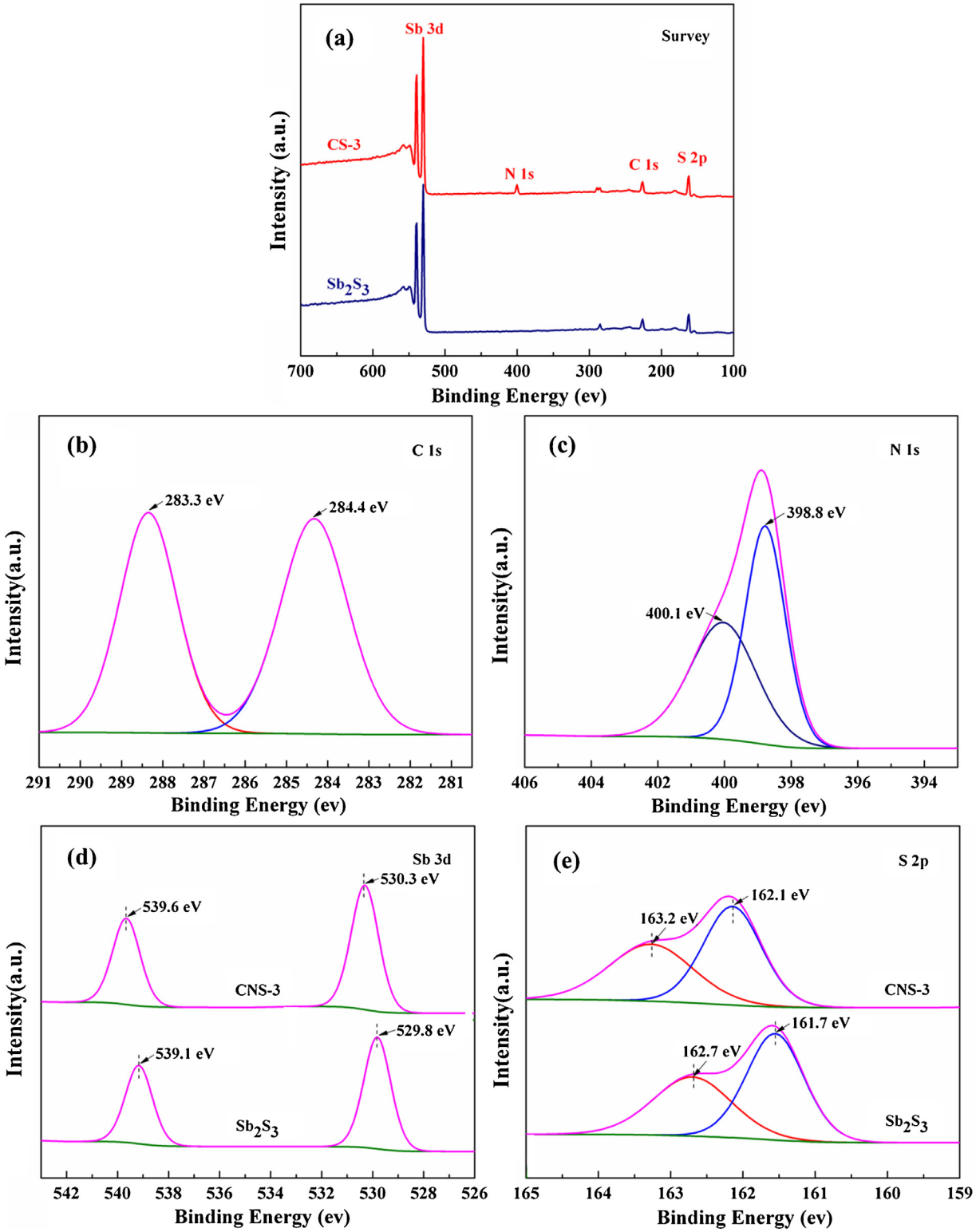

Fig. 6. XPS spectra of CNS-3 sample: (a) survey scan, (b) C 1s, (c) N 1s, (d) Sb 3d, and (e) S 2p. For comparison, the survey scan, Sb 3d and S 2p of Sb_2S_3 sample are also shown.

samples are also estimated using the following empirical equation [54]:

$$E_{VB} = X - E^e + 1/2E_g \quad (2)$$

$$E_{CB} = E_{VB} - E_g \quad (3)$$

where E_{VB} is the valence band (VB) potential, E_{CB} is the conduction band (CB) potential, X is the electronegativity of the semiconductor, E^e is the energy of free electrons on the hydrogen scale (about 4.5 eV), E_g is the band gap energy of the semiconductor [55]. The E_{VB} and E_{CB} of the photocatalysts are computed and have been integrated in Table 1. The E_{VB} of CNS composites decreased with the coupling of various CNQD-utg-C_3N_4 amounts compared with the pure Sb_2S_3, suggesting that the oxidation ability becomes stronger.

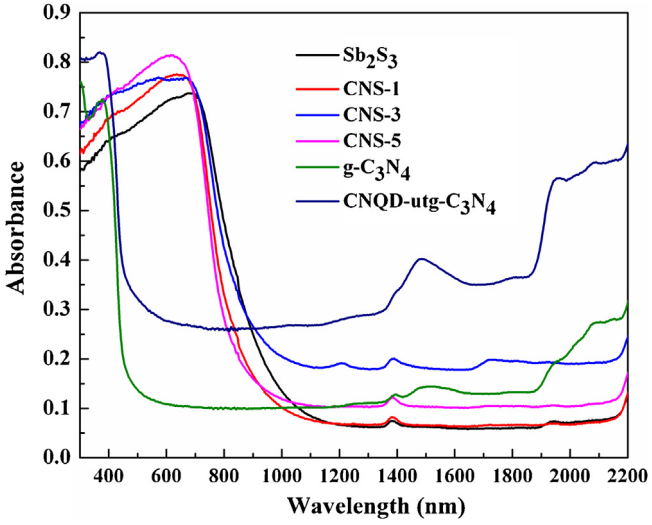

Fig. 7. UV-vis-NIR diffuses reflectance spectra of g-C_3N_4, CNQD-utg-C_3N_4, Sb_2S_3 and CNS composites.

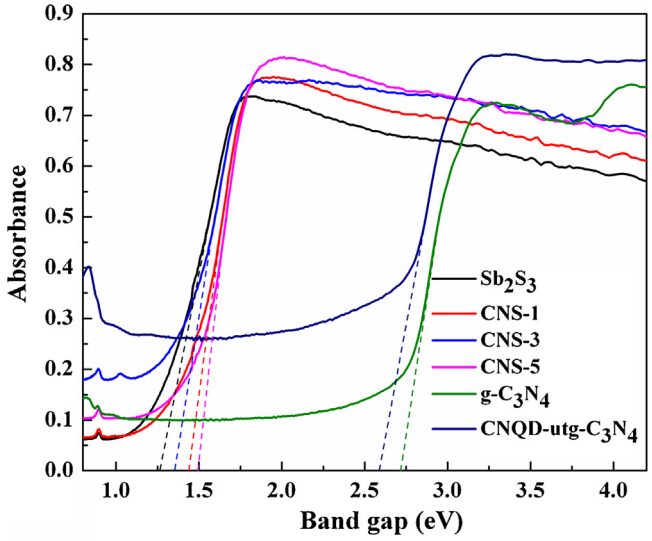

Fig. 8. The band gap energy of CNQD-utg-C_3N_4, Sb_2S_3 and CNS composites.

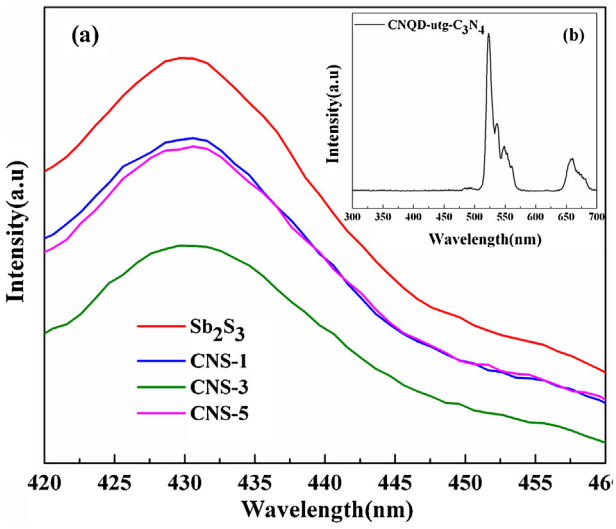

Fig. 9. Photoluminescence spectra of Sb_2S_3 and CNS hybrids (a); and the up-conversion emission spectra of CNQD-utg-C_3N_4 was recorded upon 980 nm NIR excitation (b).

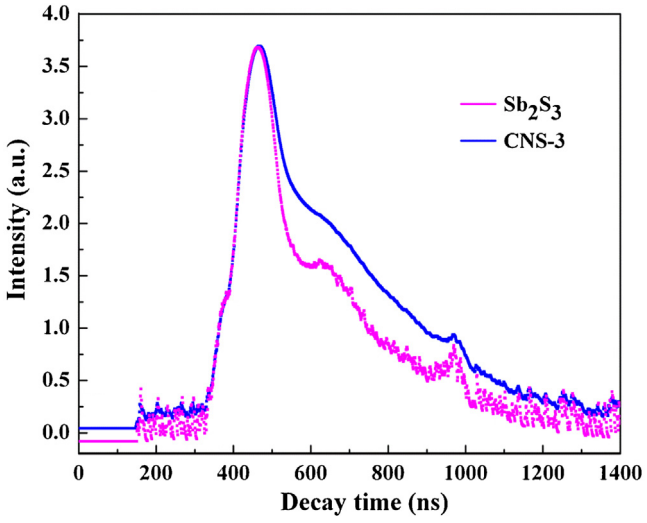

Fig. 10. The luminescence decays of the excited state levels of Sb_2S_3 and CNS-3.

To elucidate the behavior of photoinduced charge carriers, PL spectra of the photocatalysts were recorded [56]. As shown in Fig. 9, the pure Sb_2S_3 exhibits a strong, wide peak in the PL spectrum under an excitation wavelength of 370 nm. Compared with the pure Sb_2S_3, the introducing of CNQD-utg-C_3N_4 hardly changes the position of emission peak, but rather reduces its relative intensity. This clearly suggests that the recombination rate of the photo-generated electrons and holes slows down for the composite. In as-prepared CNS composites, CNS-3 possesses the lowest recombination rate of photo-generated electron-hole (e^--h^+) pairs. The inset of Fig. 9 shows the up-converted PL spectra (300–700 nm) of CNQD-utg-C_3N_4 with excitations at 980 nm (NIR light region). It is interesting to observe that the emissions are located at visible light wavelengths from 300 nm to 700 nm. The up-converted property is not observed on pure g-C_3N_4, which has been reported some papers concerned [45,52]. The multiphoton active process and anti-Stokes photoluminescence are two widespread mechanisms for the upconversion emission. Considering that the energy difference between the excitation and emission light in upconversion process is not a fixed value, the multiphoton active process may be used to explain the up-conversion emission of CNQD [8].Hence, the CNQD possesses the up-converted PL behavior and could absorb the NIR light and then convert to the visible light due to the up-conversion property. This makes the material can in reverse be excited to form the electron-hole pairs, which contribute to effectively harvesting a broad spectrum of sunshine. Consequently, the up-converted PL property of CNQD is indeed responsible for the improved photocatalytic properties of the CNS hybrid in the NIR range. This process can further be investigated by the time-resolved transient PL spectra (Fig. 10). The decay curves for Sb_2S_3 and CNS-3 can be fitted well to a double-exponential function and the corresponding lifetimes are obtained from the least square analysis [57]. The average intensity of lifetimes of Sb_2S_3 and CNS-3 were estimated to be 2.94 ns and 3.55 ns, respectively. Compared with the pure Sb_2S_3, the PL lifetime of the photoexcited electron over CNS-3 is prolonged. This facilitates the electron transport and charge-separation efficiency, which leads to a higher photocatalytic activity [38].

The linear scan voltammetry was performed under different light irradiation to investigate the light response of the CNS hybrid. From Fig. 11a, the photocurrent increases as the increasing of irradiation intensity, which contributes to enhancing density of photo-generated electrons excited by the light irradiation. To

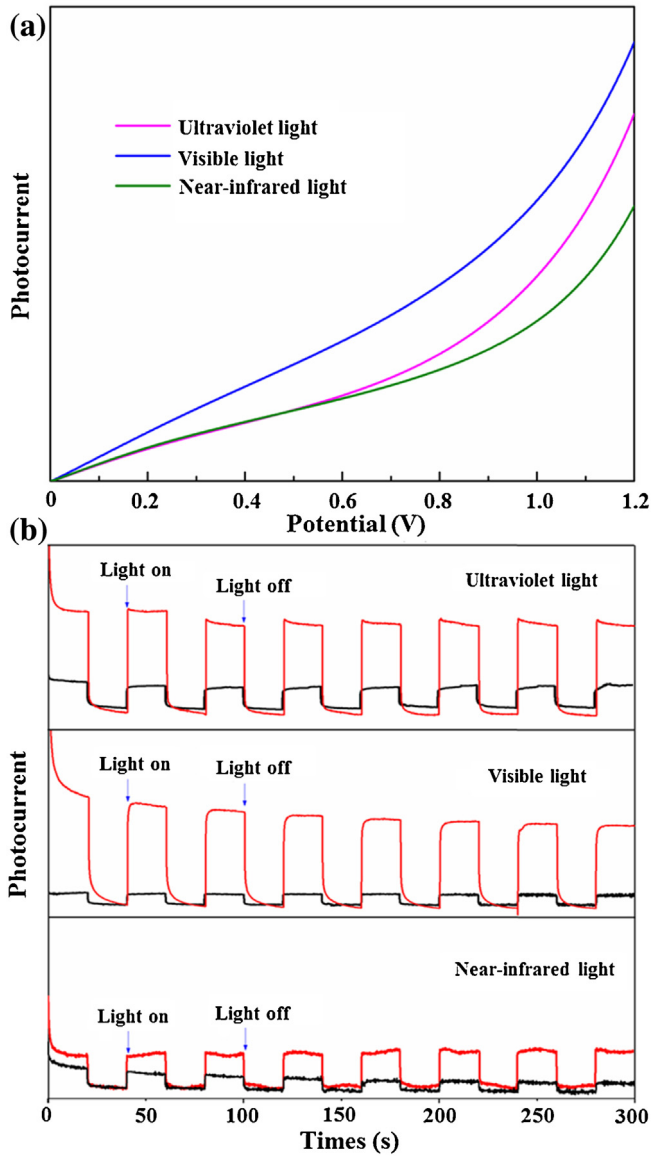

Fig. 11. (a) Typical I-V curves of the CSN-3 under ultraviolet, visible and near-infrared illumination, (b) I-T curves under chopped light illumination of Sb_2S_3 (black curve) and CNS-3 (red curve). (For interpretation of the references to colour in this figure legend, the reader is referred to the web version of this article.)

clearly investigate the variation trend of photocurrent for the CNS hybrid and the pure Sb_2S_3 with and without light irradiation, the photocurrent with chopped light is presented in Fig. 11b. The change of the photocurrent over the CNS-3 hybrid is significant under UV, visible light and NIR irradiation. The CNS-3 hybrid exhibits a higher response than the pure Sb_2S_3 under UV, visible light and NIR irradiation. This excellent photoelectrochemical performance may be ascribed to that CNQD-utg-C_3N_4 nanosheets disperse uniformly onto the Sb_2S_3 nanorods, which contributes to promoting the electron transfer between Sb_2S_3. Based on the above results, it is reasonable to believe that CNS photocatalysts have great potentiality in photocatalytic removal of pollutants, especially in the NIR-responsive photocatalysis.

3.3. Photocatalytic MO degradation

The MO photodegradation via the as-prepared CNS hybrids are evaluated under the UV, visible and near-infrared light irradiation. As the reference, g-C_3N_4 and Sb_2S_3 are tested under the same experimental conditions. Before the photocatalysis, the solution including MO and photocatalysts is stirred in the dark for 1 h to obtain the adsorption equilibrium. Under the NIR irradiation (Fig. 12a), the degradation efficiency of MO by pure Sb_2S_3 is 36% while that of g-C_3N_4 and CNQD-utg-C_3N_4 have nearly no obvious change within 120 min. When assembling CNQD-urg-C_3N_4 on the surface of Sb_2S_3 nanorods, the NIR-driven photocatalytic activity of CNS hybrids are better than that of both g-C_3N_4 and Sb_2S_3. This phenomenon can be explained by the synergistic effect between CNQD-urg-C_3N_4 and Sb_2S_3 as obtained by chemical synthesis. In particular, the optimal heterojunction photocatalysts, CNS-3, can remove 70% of MO after NIR irradiation within 120 min. To further demonstrate the relation between the photocatalytic activity of the CNS composites and excitation light, the degradation of MO under UV and visible irradiation has also been performed (Fig. 12b and c). As expected, the composites also exhibit higher photoactivity in both UV and visible irradiation, suggesting that the CNS has a wide spectral range of photocatalytic activity. The enhanced photocatalytic activity may be attributed to the stronger absorption of CNS in the light region and the efficient electron-hole separation. It is known that water itself is an absorber of electromagnetic radiation in the IR region and converts it into heat, which leads to the thermolysis of MO species. To exclude the effect of temperature, the control experiment as reference is carried out with MO solution over CNS-3 at 80 °C in the dark. Fig. 12a indicated that the decolorization rate of MO over the CNS-3 heterostructure at 80 °C is 16%. This further confirms that the near-infrared photocatalytic property of the CNS mainly due to the photocatalysis, not temperature effect or photochemical reaction caused by the NIR light. Moreover, the recycling and stability test of CNS-3 for the photocatalytic degradation of MO is depicted in Fig. 13a. It can be seen that the photocatalytic performance had no significant decrease after five cycles. This suggests that CNS-3 keeps its photocatalytic performance without distinct photocorrosion. Additionally, the XRD pattern of the CNS-3 after five times reuse is also shown in Fig. 13b. No obvious differences in the diffraction peaks are observed, confirming a very stable crystal structure. As a result, CNS-3 can be used as efficient photocatalyst for application in wastewater treatment.

To quantitatively understand the reaction kinetics of the MO degradation, the pseudo-first-order kinetics model is used to fit the photodegradation data, the equation for which is:

$$-\ln\left(C_t/C_0\right) = \mathrm{kt} \quad (4)$$

where k (min^{-1}) and t (min) are the apparent first-order rate constant and irradiation time, C_0 (mg/L) and C_t (mg/L) are the initial and remaining concentrations of MO at each time, respectively. The model fitting plots and corresponding k values are shown in Fig. 14. The order of MO degradation rate is shown in Table 2. The CNS hybrids show higher activity than that of pure Sb_2S_3 and g-C_3N_4 under the UV, visible and NIR light irradiation. It is noteworthy that with the increase of CNQD-utg-C_3N_4 content, the photocatalytic activity of the hybrids for MO degradation exhibits a rise first followed by a decline, indicating that the concentration of CNQD-utg-C_3N_4 exerts a profound influence on the photocatalytic activity. This may be caused by the fact that the excessive CNQD-utg-C_3N_4 would hinder the electrons transferring from the CNQD-utg-C_3N_4 to Sb_2S_3, and thus reducing its photocatalytic performance [35]. Several reasons may account for the improved photodegradation activity. On the one hand, the CNS composites exhibit the stronger absorption than the pure Sb_2S_3 in the NIR light region, which contributes to providing more electron-hole pairs. On the other hand, the match of lattice and energy level between the utg-C_3N_4 and Sb_2S_3 facilitates a fast electron transport, which is favorable for the efficient separation of photogenerated carriers. More importantly, CNQD can absorb NIR light, and then emit the shorter wavelength

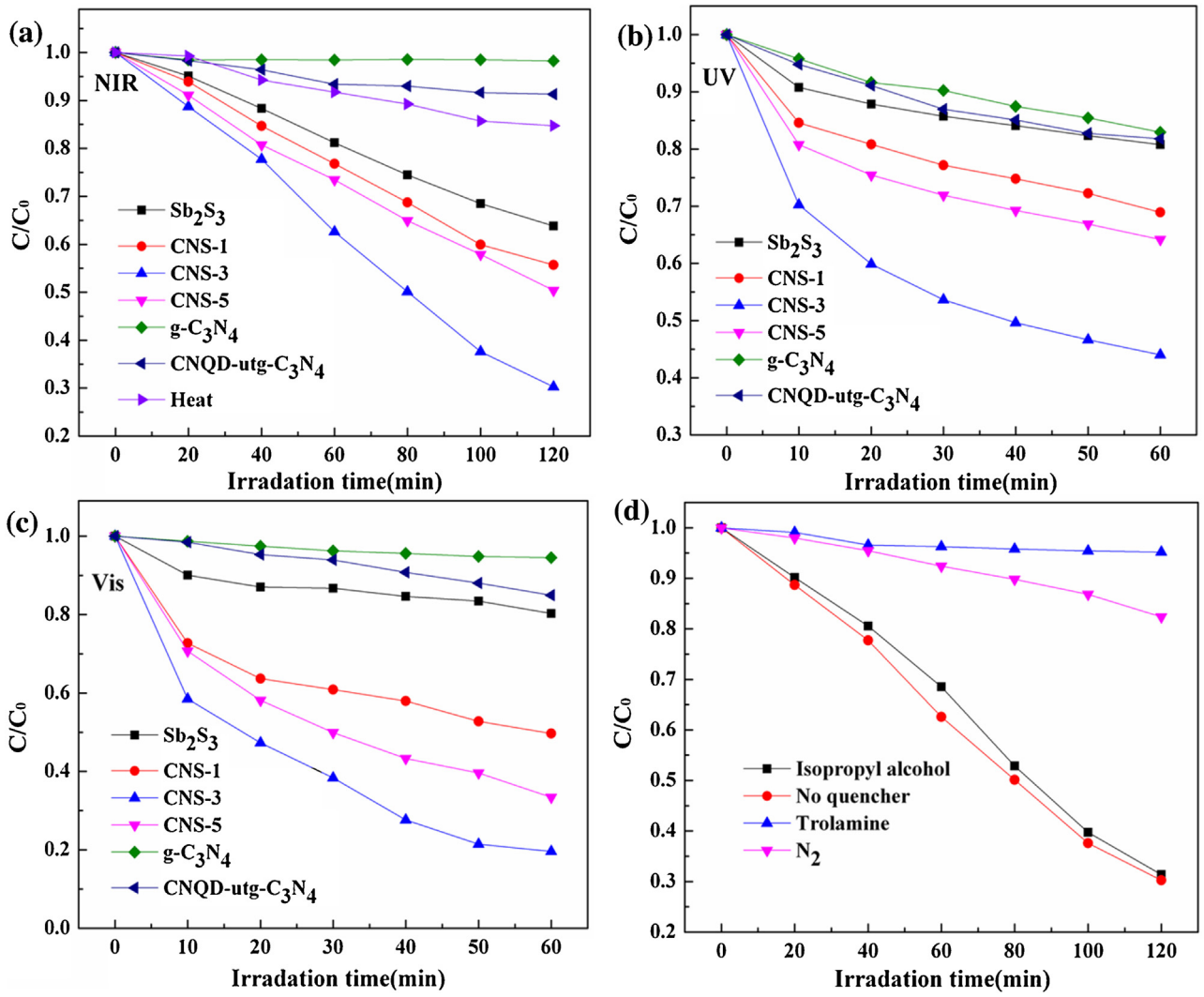

Fig. 12. MO degradation photocatalytic performance of photocatalysts under near-infrared (NIR) (a), ultraviolet (UV) (b), visible (Vis) irradiation (c). Effect of different reactive species scavengers on MO photodegradation by CNS-3 under NIR irradiation (d). The "Heat" represents the heated sample of CNS-3 at 80 °C under the darkness.

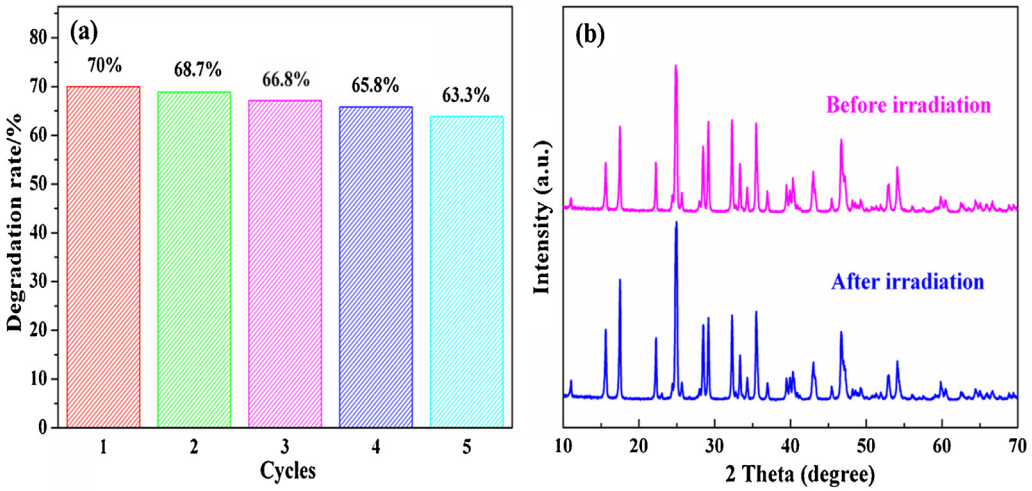

Fig. 13. Recycling tests of CNS-3 under NIR irradiation (a); The XRD patterns of the CNS-3 before and after irradiation (b).

Table 2
The corresponding k values of the model fitting plots.

Samples	Sb_2S_3	CNS-1	CNS-3	CNS-5	$g\text{-}C_3N_4$	CNQD-$g\text{-}C_3N_4$	Heat
k (min^{-1})	0.0039	0.0051	0.0103	0.0057	0.0001	0.0008	0.0015

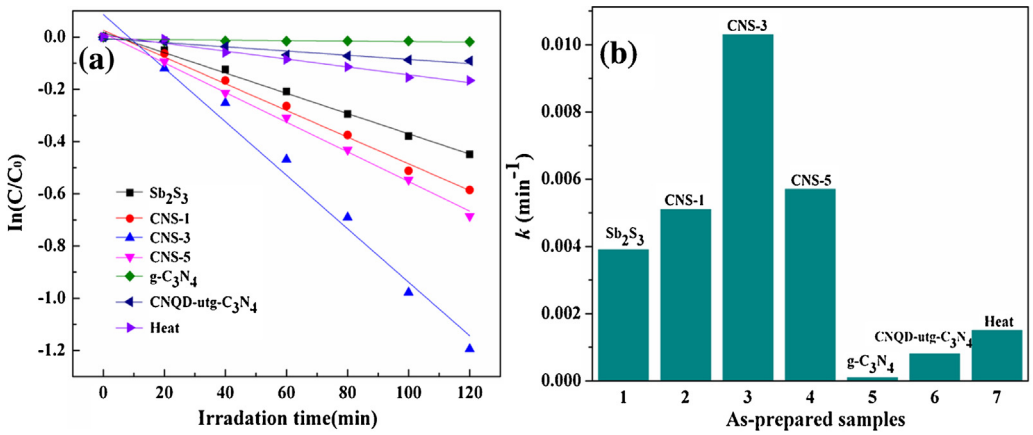

Fig. 14. The model fitting plots (a) and corresponding *k* values (b) of g-C_3N_4, CNQD-g-C_3N_4, Sb_2S_3 and CNS composites.

light due to its up-conversion PL property, which leads to the subsequent excitation of utg-C_3N_4 and Sb_2S_3, and thus enhancing the photocatalytic activities.

3.4. Photocatalytic mechanism

To investigate the possible photocatalytic mechanism, the effect of main reactive species, such as photo-generated holes (h^+), hydroxyl radicals (OH) and superoxide radical (O^{2-}), are explored in the photocatalytic process. Trolamine (TEA), isopropyl alcohol (IPA) and nitrogen (N_2) are served as the scavengers of h^+, hydroxyl radical (OH) and superoxide radical (O^{2-}), respectively [34,58,59]. After being trapped, the active species will be efficiently quenched in the MO photodegradation, and the degradation efficiency thus became lower. As shown in Fig. 12d, the photocatalytic degradation of MO is apparently suppressed after the addition of TEA and N_2. The rate constant reduces from 0.0103 min^{-1} in the photocatalytic system without any scavengers to 0.0016 min^{-1} or 0.0068 min^{-1}, when h^+ is removed by TEA or O^{2-} is not formed by N_2, respectively. Besides, ignorable inhibition is exhibited by IPA, implying the absence of OH species. Herein, the reactive species, including O^{2-} and h^+, could efficiently facilitate the MO degradation.

The band-edge potential levels play a vital role in photoexcited charge carriers in a heterojunction. To explore the mechanism of enhanced photocatalytic activity of the CNS composite, the relative band positions of the two semiconductors were investigated. The minimum CB of Sb_2S_3 is more positive than that of the g-C_3N_4, indicating that the CNS hybrid is beneficial to the separation and transportation of charge carriers. The possible mechanism is exhibited in Fig. 15, revealing the utilization of short and long wavelengths in the spectrum. When irradiated by UV and visible light irradiation, both the Sb_2S_3 and utg-C_3N_4 can be excited and generate photo-induced electrons and holes. Meanwhile, the CNQD can absorb NIR light, and then emit the shorter wavelength light due to the up-conversion property, which leads to the subsequent excitation of utg-C_3N_4 and Sb_2S_3. This enables the CNS hybrids to absorb the UV and visible light up-converted from CNQD, and thus producing the e^-/h^+. The electrons are injected from the conduction band of g-C_3N_4 to that of Sb_2S_3 due to the intimate contact between them. Instead, the holes left on the Sb_2S_3 valence band transferred to that of g-C_3N_4. The transfer of charge carrier may allow the charge separation, and then efficiently hindering the recombination of the photogenerated electrons and holes. Subsequently, the excited electrons can be captured by the O_2 adsorbed on the surface of Sb_2S_3 to form O^{2-}, which are one of the main oxidizing species to decompose MO. On the other hand, the MO molecules absorbed on the photocatalyst surface could be degraded by the separated

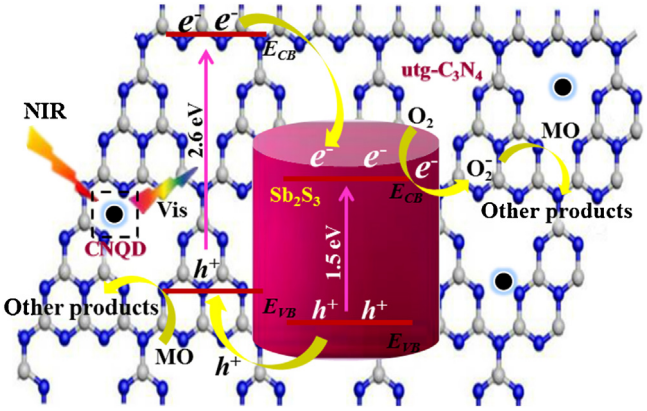

Fig. 15. Proposed mechanism for the MO degradation on the CNS composites under NIR irradiation.

holes via direct holes oxidation. The analyses are consistent with the experiment results upon the influence of radical scavengers. The above process can be described as the follows:

$$\text{CNQD+hv(NIR)} \rightarrow \text{hv(Vis)} \quad (5)$$

$$\text{utg}-C_3N_4/Sb_2S_3+\text{hv} \rightarrow \text{utg}-C_3N_4\left(e^-+h^+\right)/Sb_2S_3\left(e^-+h^+\right) \quad (6)$$

$$\text{utg}-C_3N_4\left(e^-+h^+\right)+Sb_2S_3\left(e^-+h^+\right) \rightarrow \text{utg}-C_3N_4\left(h^+\right)/Sb_2S_3\left(e^-\right) \quad (7)$$

$$e^-+O_2 \rightarrow \bullet O2- \quad (8)$$

$$h^+ + \text{MO} \rightarrow \text{otherproducts} \quad (9)$$

$$\bullet O2- + \text{MO} \rightarrow \text{otherproducts} \quad (10)$$

4. Conclusions

A series of novel CNQD-utg-C_3N_4/Sb_2S_3 composites was fabricated via a facile hydrothermal method using sodium sulfide and antimony chloride as the precursors. The CNS hybrids presented the improved photocatalytic performance for the MO degradation under UV, visible and NIR irradiation. The CNS-3 hybrid exhibited the highest NIR photocatalytic activity with MO degradation rate of 0.0103 min^{-1}, which was higher than that of g-C_3N_4, CNQD-utg-C_3N_4 and Sb_2S_3, respectively. The improved absorption in the NIR region, the efficient electron-hole separation and the up-converted PL property of CNQD were the main reasons for the improved

NIR-photocatalytic performance. The reactive species (O^{2-} and h^+) formed in the photocatalytic process led to the MO degradation. Besides, cyclic experiments indicated the photocatalysts possessed a high reusability and stability towards MO degradation. Hence, it can be concluded that the CNQD-utg-C_3N_4/Sb_2S_3 composite was a promising candidate for water treatment.

Acknowledgments

The authors gratefully acknowledge the financial support provided by Collaborative Innovation Center of Resource-Conserving & Environment-friendly Society and Ecological Civilization, the National Natural Science Foundation of China (No. 71431006, 21276069, 51521006).

References

[1] N.L. Panwar, S.C. Kaushik, S. Kothari, Renew. Sust. Energy Rev. 15 (2011) 1513–1524.
[2] H. Wang, X. Yuan, Y. Wu, Y. Liu, S. Gu, Q. Jiang, G. Zeng, Adv. Colloid Interface 221 (2015) 41–59.
[3] H. Wang, X. Yuan, Y. Wu, H. Huang, X. Peng, G. Zeng, H. Zhong, J. Liang, M. Ren, Adv. Colloid Interface 20-40 (2013) 195–196.
[4] J. Tian, Y. Sang, G. Yu, H. Jiang, X. Mu, H. Liu, Adv. Mater. 25 (2013) 5075–5080.
[5] L. Zhang, W. Wang, S. Sun, D. Jiang, Appl. Catal. B: Environ. 168–169 (2015) 9–13.
[6] C. Li, F. Wang, J. Zhu, J.C. Yu, Appl. Catal. B: Environ. 100 (2010) 433–439.
[7] H. Li, R. Liu, S. Lian, Y. Liu, H. Huang, Z. Kang, Nanoscale 5 (2013) 3289–3297.
[8] W. Wang, J.C. Yu, Z. Shen, D.K. Chan, T. Gu, Chem. Commun. 50 (2014) 10148–10150.
[9] J. Su, L. Zhu, G. Chen, Appl. Catal. B: Environ. 186 (2016) 127–135.
[10] B. Lu, J. Tang, Dalton Trans. 43 (2014) 13948–13956.
[11] N. Maiti, S.H. Im, Y.H. Lee, S.I. Seok, ACS Appl. Mater. Interface 4 (2012) 4787–4791.
[12] X.B. Cao, L. Gu, L.J. Zhuge, W.J. Gao, W.C. Wang, S.F. Wu, Adv. Funct. Mater. 16 (2006) 896–902.
[13] M. Sun, D.B. Li, W.J. Li, Y.B. Chen, Z.X. Chen, Y.H. He, X.Z. Fu, J. Phys. Chem. C 112 (2008) 18076–18081.
[14] K.Y. Rajpure, C.H. Bhosale, Mater. Chem. Phys. 64 (2000) 70–74.
[15] P.G. Sheikhiabadi, M. Salavati-Niasari, F. Davar, Mater. Lett. 71 (2012) 168–171.
[16] J. Ma, X. Duan, J. Lian, T. Kim, P. Peng, X. Liu, Z. Liu, H. Li, W. Zheng, Chem. Eur. J. 16 (2010) 13210–13217.
[17] W. Tao, J. Chang, D. Wu, Z. Gao, X. Duan, F. Xu, K. Jiang, Mater. Res. Bull. 48 (2013) 538–543.
[18] J.P. Tiwari, K. Shahi, Mat. Sci. Eng. B: Solid 141 (2007) 8–15.
[19] J. Escorcia-García, D. Becerra, M.T.S. Nair, P.K. Nair, Thin Solid Films 569 (2014) 28–34.
[20] A.V. Kozytskiy, O.L. Stroyuk, M.A. Skoryk, V.M. Dzhagan, S.Y. Kuchmiy, D.R.T. Zahn, J. Photochem. Photobiol. A: Chem. 303–304 (2015) 8–16.
[21] L. Gu, J. Wang, Z. Zou, X. Han, J. Hazard. Mater. 268 (2014) 216–223.
[22] M. Groenewolt, M. Autonienti, Adv. Mater. 17 (2005) 1789–1792.
[23] S. Ye, L.-G. Qiu, Y.-P. Yuan, Y.-J. Zhu, J. Xia, J.-F. Zhu, J. Mater. Chem. A 1 (2013) 3008.
[24] W. Zhao, Y. Guo, S. Wang, H. He, C. Sun, S. Yang, Appl. Catal. B: Environ. 165 (2015) 335–343.
[25] J.M. Xu, L. Li, S. Wang, H.L. Ding, Y.X. Zhang, G.H. Li, CrystEngComm 15 (2013) 3296.
[26] O.V. Pupysheva, Amir A. Farajian, B.I. Yakobson, Nano Lett. 8 (2008) 767–774.
[27] J. Tian, Q. Liu, A.M. Asiri, K.A. Alamry, X. Sun, Chemsuschem 7 (2014) 2125–2130.
[28] J. Tian, Q. Liu, A.M. Asiri, X. Sun, Y. He, Sens. Actuators. B: Chem. 216 (2015) 453–460.
[29] W. Ma, D. Han, M. Zhou, H. Sun, L. Wang, X. Dong, L. Niu, Chem. Sci. 5 (2014) 3946.
[30] E. Cheng, W. Yin, S. Bai, R. Qiao, Y. Zhong, Z. Li, Mater. Lett. 146 (2015) 87–90.
[31] P. Niu, L. Zhang, G. Liu, H.-M. Cheng, Adv. Funct. Mater. 22 (2012) 4763–4770.
[32] Z. Lin, J. Zheng, G. Lin, Z. Tang, X. Yang, Z. Cai, Anal. Chem. 87 (2015) 8005–8012.
[33] H. Wang, X. Yuan, H. Wang, X. Chen, Z. Wu, L. Jiang, W. Xiong, Y. Zhang, G. Zeng, RSC Adv. 5 (2015) 95643–95648.
[34] H. Wang, X. Yuan, Y. Wu, G. Zeng, X. Chen, L. Leng, H. Li, Appl. Catal. B: Environ. 174–175 (2015) 445–454.
[35] Y. Liu, X. Yuan, H. Wang, X. Chen, S. Gu, Q. Jiang, Z. Wu, L. Jiang, Y. Wu, G. Zeng, Catal. Commun. 70 (2015) 17–20.
[36] X. Yuan, Y.H. Wang, Y. Liu, X. Wu, G. Chen, G. Zeng, L. Leng, C. Zhang, Catal. Commun. 61 (2015) 62–66.
[37] Q. Guo, Y. Xie, X. Wang, S. Lv, T. Hou, X. Liu, Chem. Phys. Lett. 380 (2003) 84–87.
[38] H. Xie, W. Que, Z. He, P. Zhong, Y. Liao, G. Wang, J. Alloy. Compd. 550 (2013) 314–319.
[39] J. Zhong, X. Zhang, Y. Zheng, M. Zheng, M. Wen, S. Wu, J. Gao, X. Gao, J.M. Liu, H. Zhao, ACS Appl. Mater. Interface 5 (2013) 8345–8350.
[40] X. Wang, K. Maeda, X. Chen, K. Takanabe, K. Domen, Y. Hou, X. Fu, M. Antonietti, J. Am. Chem. Soc. 131 (2009) 1680–1681.
[41] Q. Liang, W. Ma, Y. Shi, Z. Li, X. Yang, Carbon 60 (2013) 421–428.
[42] S.J. Zhuo, M.W. Shao, S.-T. Lee, ACS Nano 6 (2012) 1059–1064.
[43] L. Jiang, H. Zeng, Nanoscale 7 (2015) 4580–4583.
[44] C. Pan, J. Xu, Y. Wang, D. Li, Y. Zhu, Adv. Funct. Mater. 22 (2012) 1518–1524.
[45] C. Han, L. Ge, C. Chen, Y. Li, X. Xiao, Y. Zhang, L. Guo, Appl. Catal. B: Environ. 147 (2014) 546–553.
[46] H. Wang, X. Yuan, Y. Wu, G. Zeng, X. Chen, L. Leng, Z. Wu, L. Jiang, H. Li, J. Hazard. Mater. 286 (2015) 187–194.
[47] S.-W. Cao, X.-F. Liu, Y.-P. Yuan, Z.-Y. Zhang, Y.-S. Liao, J. Fang, S.C.J. Loo, T.C. Sum, C. Xue, Appl. Catal. B: Environ. 147 (2014) 940–946.
[48] Q. Lv, C. Cao, C. Li, J. Zhang, H. Zhu, X. Kong, X. Duan, J. Mater. Chem. 13 (2003) 1241.
[49] Y. Cui, J. Zhang, G. Zhang, J. Huang, P. Liu, M. Antonietti, X. Wang, J. Mater. Chem. 21 (2011) 13032.
[50] Q. Han, Y. Yuan, X. Liu, X. Wu, F. Bei, X. Wang, K. Xu, Langmuir 28 (2012) 6726–6730.
[51] H. Yang, M. Li, L. Fu, A. Tang, S. Mann, Sci. Rep. 3 (2013) 1336.
[52] H. Wang, X. Yuan, Y. Wu, G. Zeng, H. Dong, X. Chen, L. Leng, Z. Wu, L. Peng, Appl. Catal. B: Environ. 186 (2016) 19–29.
[53] Y. Zang, L. Li, X. Li, R. Lin, G. Li, J. Chem. Eng. 246 (2014) 277–286.
[54] K. Katsumata, R. Motoyoshi, N. Matsushita, K. Okada, J. Hazard. Mater. 260 (2013) 475–482.
[55] H. Li, J. Liu, W. Hou, N. Du, R. Zhang, X. Tao, Appl. Catal. B: Environ. 160–161 (2014) 89–97.
[56] X. Zhou, B. Jin, R. Chen, F. Peng, Y. Fang, Mater. Res. Bull. 48 (2013) 1447–1452.
[57] X. Guo, W. Song, C. Chen, W. Di, W. Qin, Phys. Chem. Chem. Phys. 15 (2013) 14681.
[58] S. Chen, L. Ji, W. Tang, X. Fu, Dalton Trans. 42 (2012) 10759–10768.
[59] Z.H. Shah, J. Wang, Y. Ge, C. Wang, W. Mao, S.F. Zhang, R.G. Lu, J. Mater. Chem. A 3 (2015) 3568–3575.